

RESEARCH ARTICLE

10.1002/2015JD023252

Key Points:

- ARE of AAC can be quantitatively evaluated based on multisensor measurements
- Critical COD values exist to determine the signs of ARE due to AAC
- AREs are more sensitive to lower COD values than higher COD values

Correspondence to:

N. Feng,
feng@nsstc.uah.edu

Citation:

Feng, N., and S. A. Christopher (2015), Measurement-based estimates of direct radiative effects of absorbing aerosols above clouds, *J. Geophys. Res. Atmos.*, 120, doi:10.1002/2015JD023252.

Received 12 FEB 2015

Accepted 3 JUN 2015

Accepted article online 8 JUN 2015

Measurement-based estimates of direct radiative effects of absorbing aerosols above clouds

Nan Feng¹ and Sundar A. Christopher^{1,2}

¹Department of Atmospheric Science, University of Alabama in Huntsville, Huntsville, Alabama, USA, ²Earth System Science Center, University of Alabama in Huntsville, Huntsville, Alabama, USA

Abstract The elevated layers of absorbing smoke aerosols from western African (e.g., Gabon and Congo) biomass burning activities have been frequently observed above low-level stratocumulus clouds off the African coast, which presents an excellent natural laboratory for studying the effects of aerosols above clouds (AAC) on regional energy balance in tropical and subtropical environments. Using spatially and temporally collocated Moderate Resolution Imaging Spectroradiometer, Ozone Monitoring Instrument (OMI), and Clouds and the Earth's Radiant Energy System data sets, the top-of-atmosphere shortwave aerosol direct shortwave radiative effects (ARE) of absorbing aerosols above low-level water clouds in the southeast Atlantic Ocean was examined in this study. The regional averaged instantaneous ARE has been estimated to be $36.7 \pm 20.5 \text{ Wm}^{-2}$ (regional mean \pm standard deviation) along with a mean positive OMI Aerosol Index at 1.3 in August 2006 based on multisensors measurements. The highest magnitude of instantaneous ARE can even reach 138.2 Wm^{-2} . We assess that the 660 nm cloud optical depth (COD) values of 8–12 is the critical value above (below) which aerosol absorption (scattering) effect dominates and further produces positive (negative) ARE values. The results further show that ARE values are more sensitive to aerosols above lower COD values than cases for higher COD values. This is among the first studies to provide quantitative estimates of shortwave ARE due to AAC events from an observational perspective.

1. Introduction

Atmospheric aerosols can absorb and reflect solar radiation over cloudy or cloud-free regions. For example, they can increase the amount of reflected solar radiation at the top-of-atmosphere (TOA), especially above cloud-free ocean backgrounds. The change in the reflected radiative flux at the TOA between clear and aerosol regions for anthropogenic aerosols usually determines the TOA aerosol radiative forcing, while the magnitude of shortwave aerosol radiative effect (ARE) primarily depends upon surface reflectance and aerosols properties. Previous studies have mainly reported the ARE of biomass burning aerosols over cloud-free ocean backgrounds which can vary from -4 to -36 Wm^{-2} [e.g., Christopher *et al.*, 1996; Satheesh and Ramanathan, 2000; Zhang *et al.*, 2005a]. A few studies in recent years have also assessed the effects of absorbing aerosols above clouds (AAC) using a combination of satellite measurements and radiative transfer models [Chand *et al.*, 2008; Satheesh *et al.*, 2009; Wilcox, 2012; Yu and Zhang, 2013; De Graaf *et al.*, 2014; Kacenenbogen *et al.*, 2014; Peers *et al.*, 2014; Zhang *et al.*, 2014].

Conventional satellite algorithms are mainly designed for aerosol remote sensing over cloud-free regions. However, the radiative effect of AAC can still be estimated based on satellite measurements after identifying them with sensors such as the Ozone Monitoring Instrument (OMI) [Torres *et al.*, 2012] and Moderate Resolution Imaging Spectroradiometer (MODIS) [Jethva *et al.*, 2013]. Space-borne lidars (e.g., CALIOP onboard CALIPSO) can provide information about the vertical distribution of aerosols and clouds, but their swath width is inadequate for global studies [Yu and Zhang, 2013]. Once AAC are identified, cloud and aerosol properties are needed as input parameters for radiative transfer (RT) models to calculate aerosol ARE. This is also a major challenge since aerosol and cloud properties vary spatially and temporally. More importantly, the reliable quantitative retrieval of both aerosol and clouds under such situations are sparse for the estimation of ARE. Chand *et al.* [2008] estimated the diurnal ARE of aerosols above clouds, with RT calculations initialized by aerosol and cloud properties from CALIPSO and MODIS data. Wilcox [2012] assessed the diurnal ARE based on the relationship between cloud albedo and liquid water path from the Clouds and the Earth's Radiant Energy System (CERES) and Advanced Microwave Scanning Radiometer (AMSR-E) with OMI UV aerosol index (AI) constraints. Over the southeast Atlantic

Ocean (10°W–15°E, 20°S–0°S) from July to September, the ARE was reported to be $9.2 \pm 6.6 \text{ Wm}^{-2}$. *De Graaf et al.* [2012, 2014] studied the ARE of smoke aerosols over Africa by comparing simulated aerosol-free cloud reflectance from RT model with measured hyperspectral reflectance for AAC from the Scanning Imaging Absorption Spectrometer for Atmospheric Chartography (SCIAMACHY). Averaged over August 2006, the estimated ARE over the southern Atlantic Ocean near the Southern African coast was found to be $23 \pm 8 \text{ Wm}^{-2}$. Compared with previous studies, their technique has the advantage of not requiring priori assumptions of aerosols properties, although accurate parameterizations are still needed to estimate the reflectance of aerosol-free cloud scenes. Furthermore, the spatial sampling is also limited by the relatively coarse spatial resolution of SCIAMACHY. *Meyer et al.* [2013] identified AAC by using CALIOP observations and further assessed biases in MODIS-retrieved cloud properties and their impacts on ARE. The underestimation of MODIS-retrieved cloud optical depth (COD) are reported due to AAC, while the instantaneous regional mean above-cloud radiative forcing efficiency is found to increase from $50.9 \text{ Wm}^{-2} \text{ AOD}^{-1}$ to $65.1 \text{ Wm}^{-2} \text{ AOD}^{-1}$ by using their bias-adjusted MODIS cloud retrievals based on RT model calculations. Instead of assuming the aerosol properties for AAC cases, *Peers et al.* [2014] evaluated both aerosol and cloud optical properties based on multiangle total and polarized radiances measurements from Polarization and Directionality of Earth Reflectances. The direct ARE of AAC was then estimated based on RT model, which indicates the mean ARE to be 33.5 Wm^{-2} over the southeast Atlantic Ocean during August 2006. *Zhang et al.* [2014] and *Min and Zhang* [2014] used collocated MODIS cloud properties and CALIOP AAC height information to derive the subgrid cloud optical thickness for ARE computations over cloudy sky regions, while the instantaneous AAC radiative forcing efficiency is found to be $53 \text{ Wm}^{-2} \text{ AOD}^{-1}$. The importance of accurate aerosol optical properties (e.g., AOD) and underlying cloud properties (e.g., COD) has both been emphasized in their studies. However, due to tenuous aerosol layers with backscatter less than the CALIOP detection threshold, underestimations have also been reported [*Kacenelenbogen et al.*, 2014]. *Oh et al.* [2013] estimated monthly all-sky direct ARE at TOA in $1^\circ \times 1^\circ$ grids by combining measurement-based clear sky ARE and RT model calculated cloudy sky ARE based on collocated CERES and MODIS observations from Terra satellite. Although the coverage of research domain has been extended, the accuracy of results is still highly determined by the assumptions of aerosol and cloud properties in RT model. Multisensor measurement-based study for AAC events can earlier be found in *Hsu et al.* [2003], which has combined Sea-viewing Wide Field-of-view Sensor and CERES TOA fluxes along with Total Ozone Mapping Spectrometer Aerosol Index product to assess the impact of biomass burning smoke aerosols above clouds on regional energy budgets over Southeast Asia. Among recent measurement-based AAC studies, a linear relationship between AI and ARE have been widely reported, which indicates that the AI, combined with cloud optical property data, can be a good proxy for ARE estimations from a satellite perspective [e.g., *Peters et al.*, 2011; *Wilcox*, 2012; *de Graaf et al.*, 2012; *Yu and Zhang*, 2013]. Although the magnitudes of AI for AAC are only semiquantitative, the reflected radiances from the clouds would definitely vary associated with overlaid aerosol particles layer. Satellite-reported AI is found to be sensitive to absorbing aerosols above clouds but also be related to other issues such as underlying cloud properties and vertical distributions of aerosol and clouds layers. However, those satellite retrieved aerosol and cloud properties (e.g., AI and COD) from multisensors have to be dealt cautiously, since the impact of absorbing aerosols above clouds on remotely sensed aerosol and cloud properties retrievals has been widely recognized and quantitatively assessed by recent studies [*Meyer et al.*, 2013; *Jethva et al.*, 2013; *Alfaro-Contreras et al.*, 2014].

In this study, we assess the ARE for AAC based on multisensor observations from A-Train data sets [*L'Ecuyer and Jiang*, 2010] including the MODIS and pixel-level CERES on Aqua and OMI on Aura. To our knowledge, this is the first attempt at combining pixel-level CERES radiative fluxes, OMI aerosol index, and MODIS cloud optical depth to assess ARE due to AAC events, although *Oh et al.* [2013] used level 3 gridded CERES data to evaluate all-sky ARE. For those AAC pixels, OMI can be used to detect the presence of absorbing aerosols. Further, instead of using RT calculations, we collocate the CERES pixels with OMI and MODIS to obtain TOA shortwave fluxes, while realizing that proper angular models are not yet available to convert radiances to fluxes for the case of AAC. The MODIS $1.6 \mu\text{m}$ COD product (with less effect due to submicron aerosols) has been used to provide underlying cloud properties, since previous studies have reported 30–50% underestimations of near-IR ($0.86 \mu\text{m}$) MODIS COD retrievals due to absorbing aerosols

Table 1. Multisensors, Parameters, and Their Corresponding Spatial Resolutions in the Study

Satellite	Sensor	Parameter	Nadir Spatial Resolution	Data Availability
Aqua	MODIS	COD, R_e , temperature, cloud fraction,	1 × 1 km 1 × 1 km 5 × 5 km	2002 to current
Aqua	CERES	Radiance, radiative flux, albedo, cloud fraction, and cloud phase	20 × 20 km	2002 to current
CALIPSO	CALIOP	Cloud top height, cloud layer flag, and aerosol top/base heights	5 × 5 km (vertical 30 m)	2006 to current
Aura	OMI	UV aerosol index	13 × 24 km	2004 to current

above clouds [e.g., Haywood *et al.*, 2004; Meyer *et al.*, 2013; Jethva *et al.*, 2013; Alfaro-Contreras *et al.*, 2014]. We also provide uncertainty and sensitivity analysis on the assumptions and methods that are being used in this study.

2. Data and Methods

In this section, we provide a brief description of the A-Train data sets, data fusion techniques, and RT model calculations that are used for this study. We primarily focus on AAC cases over the southeast Atlantic Ocean during August 2006–2010, where strong absorbing smoke aerosols from southwestern African countries of extensive rainforests and savannah burning lie above the highly reflective stratocumulus cloud. This is one of the world’s largest biomass burning source and presents an excellent natural laboratory for studying the effects of absorbing aerosols due to AAC events on regional energy balance in tropical and subtropical environments. Table 1 contains a description of the A-Train satellites and their characteristics used for this study.

2.1. Aqua-MODIS

MODIS has 36 spectral (0.405 μm –14.385 μm) channels with a swath width of \sim 2400 km with a near daily global coverage. We use the most recently available level 2 (Collection 6) cloud products (MYD06_L2) to obtain spatial distribution of COD [King *et al.*, 1997]. Spectral and spatial measurements used to identify clouds retrievals over land and ocean are from separate algorithms with a spatial resolution of 1 or 5 km [Baum *et al.*, 2012]. As has been mentioned above, standard MODIS COD retrieved at near-IR channel (0.86 μm) can be largely underestimated during AAC events, since absorbing aerosols reduce the reflected solar radiation from the underlying clouds. Hence, MODIS COD based on 1.6/2.1 μm channels (COD_1621) are used in this study, which has been suggested to be less affected by above-cloud fine-mode aerosol particles (e.g., biomass burning smoke) than the standard MODIS cloud product [Alfaro-Contreras *et al.*, 2014]. COD_1621 are retrieved based on SW IR channels (1.6/2.1 μm) and again are referenced back to the visible channel (0.66 μm).

2.2. Aura-OMI

OMI onboard Aura provides high-resolution spectral ultraviolet (UV) bands from 0.27 μm to 0.5 μm with a spatial resolution of 13 × 24 km at nadir. This study uses the Aura OMI/OMAERUV level-2 version 3 product. Major advantages of using OMI include their capabilities of capturing absorbing aerosols in the near-UV channels which can be further used for retrieval of aerosol properties over both land and water surfaces due to low UV surface albedo of all ice-snow-free surface features [e.g., Torres *et al.*, 2007]. Previous studies have shown that smoke and dust aerosols have larger absorption AOD at short wavelengths (near UV) than longer wavelengths [e.g., Russell *et al.*, 2010]. Their perturbations to upward radiance by underlying brighter surface such as clouds or deserts in different wavelengths can be detected by absorbing aerosol index (AI) from OMI observations in the UV range [Yu and Zhang, 2013]. OMI AI is computed based on the differences between remotely observed radiances for real scenarios and RT model calculated radiances for Rayleigh-scattering atmosphere in UV bands [Krotkov *et al.*, 1998; Hsu *et al.*, 1999]:

$$AI = -100 \left[\log_{10} \left(\frac{I_{360\text{nm}}}{I_{330\text{nm}}} \right)_{\text{meas}} - \log_{10} \left(\frac{I_{360\text{nm}}}{I_{330\text{nm}}} \right)_{\text{calc}} \right] \quad (1)$$

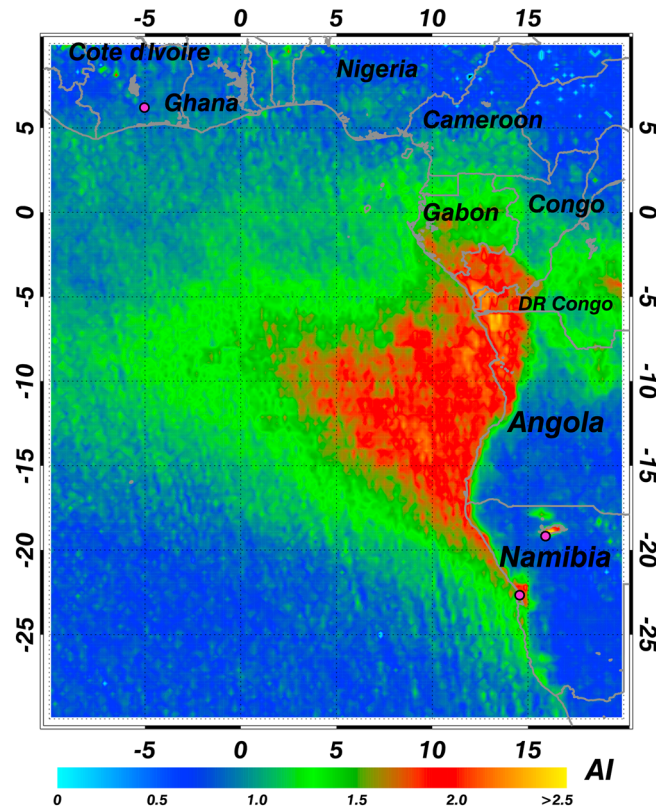


Figure 1. Area of study with the contour map of gridded averaged OMI aerosol index during August from 2006 to 2010.

at nadir with much larger footprints near the edge of nadir. We use the latest CERES Single Scanner Footprint TOA/Surface Fluxes and Clouds (SSF) product, which contains instantaneous pixel level data for a single scanner that is collocated with high-resolution MODIS imager on Aqua (CER_SSF_Aqua-FM3-MODIS_Edition 3A). In this product, the higher-resolution MODIS data such as scene identifications and cloud and aerosol properties are averaged over the larger CERES footprint using point spread functions [Smith, 1994]. Our group has experience in such measurement-based analysis for clear sky ARE of aerosols estimations over oceans [Zhang *et al.*, 2005a, 2005b] and over land [Patadia *et al.*, 2008; Feng and Christopher, 2014].

2.4. CALIPSO-CALIOP

CALIOP onboard CALIPSO (Cloud-Aerosol Lidar and Infrared Pathfinder Satellite Observations) measures backscatter vertical profiles at 532 and 1064 nm during both day and night, which gives information on the vertical location of clouds and aerosols as they have higher backscatter values than the background clear sky [Vaughan *et al.*, 2004]. Then, the color ratio [1064/532 nm total attenuated backscatter] and depolarization ratio (perpendicular/parallel channels at 532 nm) profiles help to distinguish between cloud and aerosol. Clouds generally have larger color ratio values than dust aerosols because 1064 and 532 nm backscatter measurements for clouds are often similar in magnitude due to the larger particles [Liu *et al.*, 2004].

In order to produce the level 2 CALIPSO product, cloud and aerosol layers are first located using a set of algorithms applied to the level 1 (L1) 532 nm backscatter profiles known as the selective, iterated boundary locator (SIBYL) [Winker *et al.*, 2009]. SIBYL provides the height of cloud and aerosol layers (physical properties) by scanning CALIOP profiles to detect features and averaging profiles and removing detected layers from the profiles before further averaging. The latest version 3 product uses a 5-degree probability distribution function approach which incorporates the depolarization ratio and latitude along with the backscatter, color ratio, and layer center altitude [Zhang *et al.*, 2014]. Recent studies reveal that

where I represents the upwelling radiance at TOA for two different UV wavelengths in the range of weak gaseous absorption. A positive AI value indicates the presence of an elevated absorbing dust or smoke layer in clear scenes or above clouds, zero, or small negative AI indicates Rayleigh-scattering atmosphere, clouds, and scattering aerosols. Figure 1 shows the area of this study and the gridded-average OMI AI during August between 2006 and 2010. Note that OMI measurements that have been flagged as row anomalies have been removed during processing in this study. High AI values (>0.5) indicating the presence of elevated absorbing aerosols can be observed from Southwest African coast to south Atlantic Ocean, which is also confirmed by previous studies [e.g., Yu *et al.*, 2012].

2.3. Aqua-CERES

The TOA broadband SW and LW radiances measured by Clouds and Earth Radiant Energy System (CERES) instruments [Wielicki *et al.*, 1996] are converted to fluxes using angular models. The pixel resolution is ~ 20 km

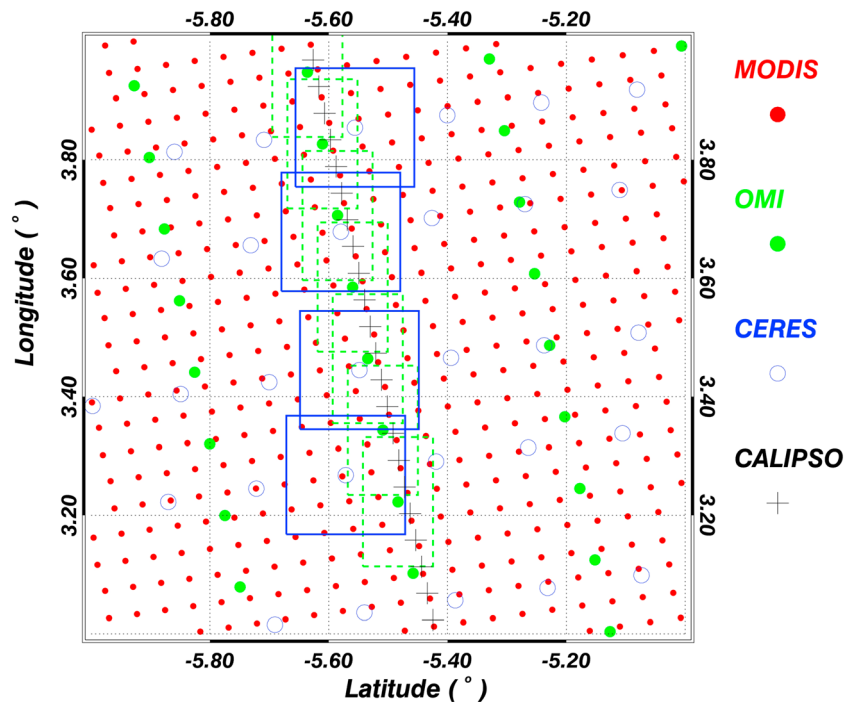


Figure 2. Latitude and longitude of MODIS, OMI, and CERES pixels for a small portion of the swath with examples for collocations of CERES, OMI, MODIS, and CALIOP pixels. The CERES pixel is assumed to be blue dash rectangular with a blue unfilled circle in the center. The location of MODIS pixel is shown by a small red filled circle and OMI pixel by a medium filled green point with green dash parallelogram. CALIPSO pixels are shown by black plus signs, which can provide vertical profiles in a very limited area.

the version 3 product is significantly more accurate in correctly classifying dense dust and smoke plumes due to the inclusion of the depolarization ratio and latitude [Winker *et al.*, 2010; Zhang *et al.*, 2014].

2.5. Data Fusion

We provide a data fusion framework here since multiple sensors will be used. The fundamental assumption is that the pixel of interest does not undergo changes in surface, cloud, aerosol, or atmospheric properties during the time of the overpass of the Aqua, Aura, and CALIPSO since they are within seconds to minutes of one another. However, the spatial resolutions of these data products are different. In general, when using multiple data sets of different spatial resolutions, the final product will assume the coarsest spatial resolution, but the information content and the inference capability will be improved. Since our final goal is to provide a data set that will provide a product that can assess the role of aerosols in cloudy regions, we use the CERES as a base line sensor. For MODIS cloud product, pixels with cloud cover fraction above 95% have been selected, while only 1 km scenes with both available standard (0.86 μm) and supplementary (1.6/2.1 μm) COD retrievals have been applied to avoid missing lines in the data due to dead detectors [Alfaro-Contreras *et al.*, 2014]. The CERES and OMI AI data quality with the highest confidence are selected. Figure 2 shows a small section of the MODIS, OMI, CERES and CALIOP swath from NASA A-Train satellite with approximately the same overpass time, which indicates the relative size of each pixel, along with a track of CALIOP pixels. It also shows the collocation procedure for one CERES pixel and the corresponding MODIS and OMI pixels, while the size of each MODIS, OMI, and CERES pixel is indicated and is approximately equal to the dimensions at nadir. Along with all available vertical profiles of aerosols and clouds from CALIOP, daily OMI AI, MODIS COD (τ), and CERES SW Fluxes are collocated within $0.2^\circ \times 0.2^\circ$ (latitude \times longitude) bins. Next, the AAC pixels are only identified by those grids with both AI > 0.5 and COD > 0 . The ARE is then calculated by subtracting CERES SW flux (where AAC are present) from aerosol-free cloudy sky flux (equation (2)):

$$\text{ARE} = F_{\text{cld}} - F_{\text{cld} + \text{aer}} \quad (2)$$

The radiative fluxes for aerosol-free cloudy sky (denoted as F_{clid}) are estimated on a pixel-by-pixel basis by assuming that a linear relationship exists between AI and TOA fluxes for each COD bin from 0 to 32. F_{clid} is then reported under OMI AI baseline values representing no aerosol above cloud conditions for each COD bin. $F_{\text{clid+aer}}$ denotes the TOA fluxes for AAC pixels that are identified based on collocated OMI, MODIS, and CERES observations.

2.6. Radiative Transfer Calculations

Previous studies have shown extensive uncertainties among various satellite-retrieved aerosol and cloud properties (e.g., AI and COD) under complex AAC conditions. [Yu *et al.*, 2012; Meyer *et al.*, 2013; Jethva *et al.*, 2013; Alfaro-Contreras *et al.*, 2014]. In order to quantify how these errors would impact the estimation of ARE due to AAC events, several sensitivity studies have been conducted by performing a Discrete Ordinate Radiative Atmospheric Radiative Transfer (SBDART) model calculations. This discrete ordinates radiative transfer computer code can be used to characterize the atmospheric radiative effects under various scenarios with or without aerosols above cloud. The sun-satellite viewing geometry, spectral dependence of aerosol properties, vertical distributions of aerosol and cloud layers, and other parameters are taken as input to perform the computation. The SBDART model is used in this study to find quantitative correlations among aerosol and cloud properties. The RT retrieved AI is calculated based on equation (1) mentioned in section 2.2. A delta-four stream plane-parallel broadband RT model [Fu and Liou, 1993] is also used to compute shortwave (0.17–4 μm , divided by 15 SW bands) flux and ARE values for AAC scenarios to determine how well the model and satellite data sets compared against each other. The assumptions of input parameters for the both RT models include the surface albedo (ocean only); the default tropical atmospheric profiles [McClatchey *et al.*, 1971] of water vapor, temperature, and other atmospheric constituents (e.g., O_3); averaged surface pressures based on available sounding measurements; the height of aerosol and cloud layers; and wavelength dependent aerosol optical properties (e.g., single-scattering albedo (ω_0), extinction coefficient (β_{ext}), and asymmetry factor (g)). Strong seasonal variations of aerosol's ω_0 associated with biomass burning activities have been observed from Aerosol Robotic Network (AERONET) retrievals at sites in Southern Africa, while the lower ω_0 of 0.81 at 0.55 μm at the beginning of July can largely increase to 0.92 by the end of November based on 15 years of ground observations in Mongu, Zambia [Eck *et al.*, 2013]. In Figure 3, aerosol properties (filled circle) in RT model calculations are obtained from ground-based measurements from AERONET level 2.0 data over Mongu, Zambia (15.254°S, 23.151°E) during selected period with ω_0 , τ , and g at 0.55 μm for smoke aerosols as 0.87, 0.33, and 0.60 respectively. The wavelength-dependent aerosol properties are then interpolated or extrapolated into RT model wavelengths (open circles) based on empirical equations from previous studies [Reid *et al.*, 2005a, 2005b; Wang and Christopher, 2006]. According to the AAC cases detected by CALIPSO during the study period, the maximum concentration of aerosol layers are found to be varied from 1.6 km to 5.0 km with an average height of 4.2 km, while cloud layers are found between 0.9 km and 3.4 km with an average height of 1.8 km. Hence, the top heights of both aerosol and cloud layer are assumed to be 4.2 km and 1.8 km in RT calculations, respectively. Results from RT model are only used to quantify those errors and sensitivities of various impact factors (e.g., AI, COD, and layer heights) in the process of our measurement-based above-cloud ARE estimations, because it is hard to capture accurate above-cloud aerosols optical properties (e.g., ω_0 , β_{ext} and g) and vertical profiles over the ocean without field campaigns.

3. Results and Discussion

3.1. Estimations of ARE for AAC Based on Multisensor Measurements and Radiative Transfer Calculations.

In Figure 4a, the relationship between SW flux at TOA and AODs (colored, filled-in circles) as a function of COD are first assessed based on RT calculations, which has been separated into the same COD bins in Figures 4b and 4c. Note that the aerosol optical properties (see in Figure 3) from ground-based measurements are used in the RT model, along with assumed atmospheric conditions, ocean surface (surface albedo $\alpha_{0.55\mu\text{m}} = 0.07$), cloud properties, and heights of clouds and aerosols. Variations of TOA shortwave flux for AAC show an increasing (decreasing) trend along with increase of AOD for low (high) COD values. This is consistent with statements from previous studies that ARE due to absorbing aerosols above clouds are determined by both aerosol and cloud properties, especially above ocean backgrounds [Yu and Zhang, 2013].

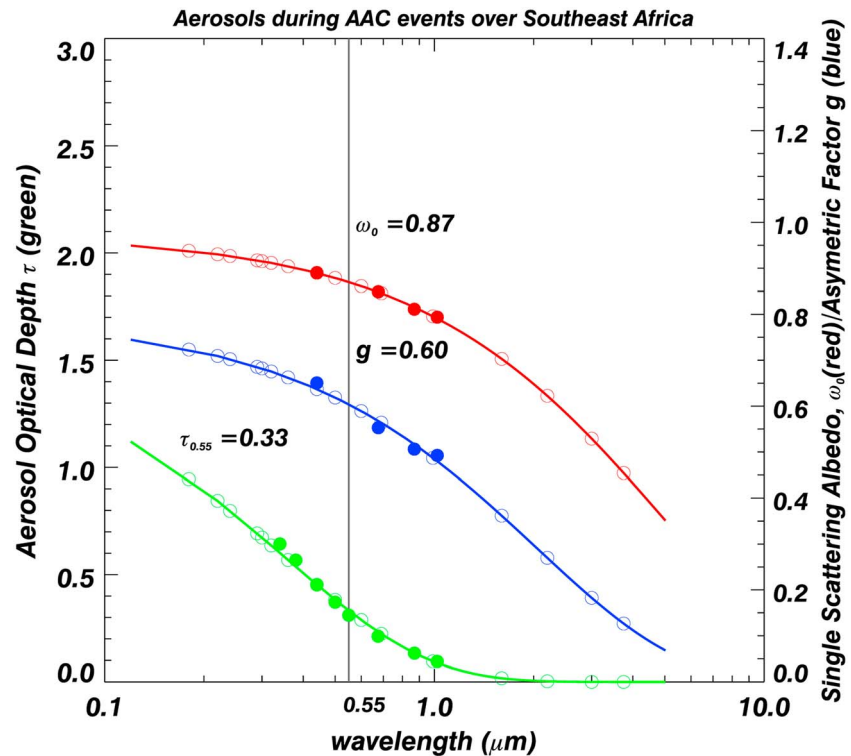


Figure 3. Wavelength-dependent aerosols optical depth (green), single-scattering albedo (red), and asymmetric factor (blue). Filled circles are derived from the AERONET sun photometer measurements during August 2006 at Mongu, Zambia (15.254°S, 23.151°E), while these data have been exponentially fitted to calculate the parameters at wavelengths in the RT model (unfilled circles). The numbers labeled in the figures are the values of these parameters at 0.55 μm. The data in this figure is applicable for both SBDART and Fu-Liou in this study.

Yu *et al.* [2012] indicated the linear relationship between above-cloud AOD and AI as a function of COD by using 8 months of A-Train measurements of absorbing aerosols and cloud properties from Southwest African smoke outflow regions. Based on multisensor measurements in this study, Figure 4b describes the relationships between collocated OMI AI and CALIPSO above-cloud AOD in various Aqua MODIS COD bins, which can be further used to derive the OMI AI baseline values for aerosol-free cloud conditions [Yu *et al.*, 2012]. Higher UV AI from OMI can be seen along with increasing above-cloud AOD from CALIPSO for most COD bins, while the AI can also be affected by the underlying COD. For a low above-cloud AOD around 0.02, the AI can reach as high as 2.5 with large COD values between 20 and 32. Previous studies have also presented that AI magnitude for AAC events depends on aerosol properties (i.e., AOD, wavelength dependent ω_0 , and angstrom absorption exponent), underlying cloud properties (e.g., COD), and vertical distributions of both aerosol and cloud layers [Torres *et al.*, 2012; Yu *et al.*, 2012; Alfaro-Contreras *et al.*, 2015]. The latest study of Alfaro-Contreras *et al.* [2015] has conducted a first examination of baseline CALIOP above-cloud AOD and OMI AI thresholds (AOD=0.015 at 0.532 μm; AI=1.0) to distinguish clean background from significant AAC events based on both global and regional measurements. In this study, the AI threshold for AAC events are selected to be 0.5, where most above-cloud CALIOP AODs for the AAC events over our study domain are under 0.015 at 0.532 μm. It can be further seen in Figure 4c that there are excellent relationships between OMI AI and CERES SW flux as a function of MODIS COD values over the area of study. To examine the effect of AI and COD, we bin the CERES SW flux and AI according to various COD ranges. In Figure 4c, data from multisensor measurements (shown in gray pixels as background) appear rather noisy at first glance, although a general decrease in SW flux is seen as a function of AI for AAC with high COD values ($12 < \tau < 32$), while the SW flux can also be seen to increase with AI for AAC with low COD values ($0 < \tau < 8$). The slope between SW fluxes and AI is around zero for ($8 < \tau < 12$). Previous studies have shown that the change in SW flux is a combined effect of both the aerosols and the underlying surface properties [Patadia *et al.*, 2009].

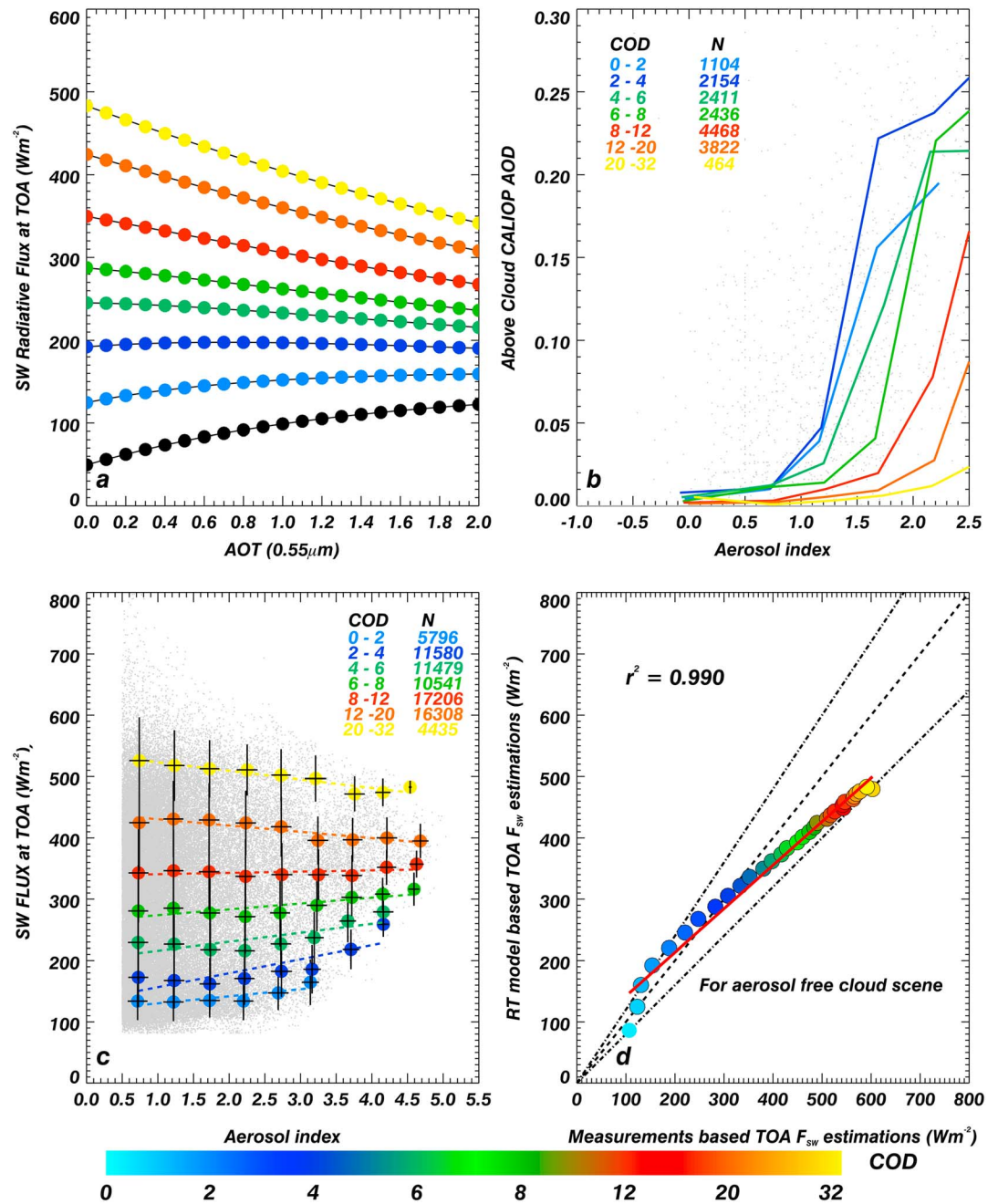


Figure 4. (a) Relationship between TOA shortwave flux (SWF) and aerosol optical depth (AOD) as a function of cloud optical depths (COD) based on results from the four-stream RT model calculations for biomass-burning smoke aerosols at SZA = 35° and VZA = 40°. (b) Comparison between collocated OMI AI and CALIOP observed above-cloud AOD as a function of the underlying MODIS COD. CALIOP AOD is averaged into OMI AI bins of 0.1. (c) Relationship between TOA SWF from CERES and estimated AI from OMI as a function of COD from MODIS. The colored lines and filled circles show the SWF-AI relation based on each COD bins, and the gray points on the background are pixel level data from measurements. (d) The comparisons of TOA SW fluxes for aerosol-free cloud scene based on RT model estimations and A-Train measurements.

From Figure 4c, it is apparent that for our study region during August, the COD values of 8–12 appear to be the critical COD below (above) which aerosol-scattering (absorbing) effect dominates. Similar results have been shown in a recent study for dust and smoke aerosols above clouds based on the radiative transfer calculations [Jethva et al., 2013]. They reported an increase in AOD results in increased TOA reflectance for lower COD values ($\tau < 10$) due to aerosol scattering effects, while the absorption of cloud-reflected radiation due to AAC dominates their scattering effect for higher COD values ($\tau > 10$). Much lower critical COD values

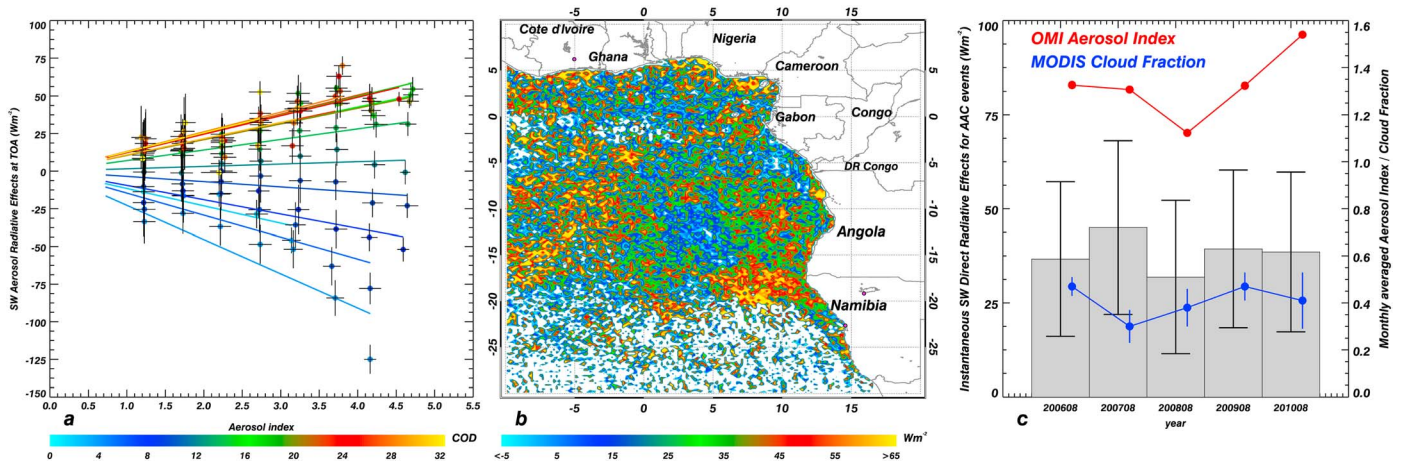


Figure 5. (a) Relationship between collocated OMI AI and TOA SW ARE as a function of various COD bins based on measurements. (b) Gridded mean instantaneous (i.e., time of observation) above-cloud direct aerosol radiative effect (ARE) at TOA averaged over August 2006 based on OMI/MODIS/CERES collocated data sets, for cloudy MODIS pixels for which OMI AI product produces a reliable above-cloud highly absorbing aerosol retrievals. Purple points are AERONET sites over the land. (c) Histograms of monthly area-averaged above-cloud aerosols SW ARE along with OMI AI and MODIS cloud fraction in the study region for 2006–2010. Standard deviations of the bars are based on regional statistics.

can be found among simulation results for carbonaceous aerosols above clouds [Jethva et al., 2013]. This confirms that the variation in TOA shortwave fluxes can be interpreted as the combined response to both variations in COD and AOD [De Graaf et al., 2012, 2014; Jethva et al., 2013]. The variation in SW flux with AI is of interest because of the ARE due to these aerosols above cloudy regions, which can be calculated based on satellite measurements. In Figure 4d, the estimated TOA shortwave fluxes for pure cloud scenes (AI=0.5) are compared with RT model calculations for each COD bin. The dashed lines represented the $\pm 10\%$ error lines and 1:1 ratio lines, respectively. The close agreements between measurement and model-based estimations indicate lower uncertainties of estimated TOA SW fluxes for aerosol-free cloud scene from observations.

In Figure 5a, we calculate the ARE and analyze it as a function of COD. As mentioned above, for $COD < 8$, where the scattering effects of aerosols dominate, ARE values are shown to be negative which is a cooling effect. For $COD > 12$, the aerosols predominantly absorb both incident and reflected solar radiation and will cause positive ARE (warming effects), compared to aerosol-free cloud backgrounds. Thus, depending on the range of COD and AI values, ARE values of AACs can be calculated based on the estimated shortwave flux from aerosol-free cloud scene when AI is less than 0.5 for each COD bin. The variability of the AI, as a function of sun-solar-viewing geometry and aerosol-layer heights, is responsible for some of the spread in the data of ARE for AAC, causing it to influence the total range of absolute ARE values. The physical reasons for the deviations from the linear fit at high ARE are unclear, especially since above-cloud aerosol ARE is probably underestimated for high values. This is because the CERES SSF product applied the cloud angular distribution models types to convert the SW radiance to flux, instead of using accurate AAC scene, causing errors in estimations of the SW Flux for AAC and further results in the uncertainties of the ARE. Besides, the large deviations over high AI ranges can also be caused by the nonlinear relationships between AI and the amount of aerosols or aerosol absorption optical thickness for higher AI values [de Graaf et al., 2012] (seen also in Figure 4b). The regionally averaged above-cloud ARE was then calculated over the south Atlantic Ocean between 20°S–10°N and 10°W–20°E (ocean only) in August 2006–2010. Figure 5b shows spatial variations in ARE due to aerosols above clouds, which is a largely measurement-based assessment. A few regions shown in red or yellow over the ocean representing peak values are caused by the low sampling of data but most is due to the variable cloud and aerosols fields, which change rapidly in short time periods. The greatest concentrations of AAC (monthly averaged AI > 1.5) with strongest positive (warming) effects ($> 35 \text{ Wm}^{-2}$) lie just west of the Southern African coast, between 0 and 15°E. This finding is consistent with previous studies using both satellite observations and RT model calculations [de Graaf et al., 2012, 2014; Meyer et al., 2013]. De Graaf et al. [2012] indicated that the estimated ARE over the south Atlantic Ocean near the Southern African coast was $23 \pm 8 \text{ Wm}^{-2}$ during August 2006. Meyer et al. [2013] reported the instantaneous regional mean above-cloud radiative forcing efficiency to increase from $50.9 \text{ Wm}^{-2} \text{ AOD}^{-1}$ to $65.1 \text{ Wm}^{-2} \text{ AOD}^{-1}$ by using their bias-adjusted MODIS

cloud retrievals based in RT model calculations. More recently, by using SCIAMACHY observations and RT model calculations, *De Graaf et al.* [2014] estimated SW aerosol direct radiative effects to be $30\text{--}35\text{ Wm}^{-2}$ over the same domain in August and September 2006–2009. In this study, the maximum ARE in August 2006 was 138.2 Wm^{-2} , while the regionally and monthly averaged value was 36.7 Wm^{-2} with a regional standard deviation of 20.5 Wm^{-2} during August 2006. A little higher ARE due to AAC events are found in our A-Train satellite measurement-based estimations than the previous studies mentioned above, which might be mainly due to different estimation processes for the aerosol-free cloud scene. Lower SW fluxes for the aerosol-free cloud scene in this study are retrieved from the linear approximation of multisensor measurements, while simulated aerosol-free cloud reflectance corresponding to high SW fluxes for the scene is used in *De Graaf et al.* [2012, 2014]. The variations of the instantaneous ARE due to AAC events along with monthly OMI AI and MODIS cloud fraction in this area during August 2006–2010 are also given in Figure 5c, while the height and the error bars indicate the regional mean and standard deviation, respectively. Comparing to the year of 2006, the available aerosol above-cloud collocated points have been reduced by 46.7%, 26.3%, and 14.72% from 2007 to 2009, which is largely associated with row anomaly occurred for mostly nadir-viewing scenes OMI data since 2007. It is also consistent with the current OMI row anomalies online report that few data reductions can be seen in 2010. The monthly averaged AI during AAC events are not seen to be affected by this data missing problem, since it only slightly varied from lowest value of 1.12 in 2008 to the highest value of 1.54 in 2010. As a dimensionless quantity, one AI unit has been reported to indicate about 2.3% radiance change with a regular sensor noise of about 0.2 AI units [*Torres et al.*, 2002]. Strong SW ARE due to peak absorption of biomass burning smoke aerosols during AAC events in August 2007 is consistent with recent study performed by *De Graaf et al.* [2014]. Larger standard deviations of spatial distributions are found in 2007 and 2010 than other years, which indicate more regional discrepancies. In general, these measurement-based estimations are well matched with related studies over south Atlantic Ocean near the South African coast during recent years, which indicate that steady warming effects due to biomass-burning aerosols above water clouds are highly different with previous reports for negative cooling effects due to smoke aerosols over clear sky in both signs and magnitude [e.g., *Christopher and Zhang*, 2002]. By assuming an absorbing aerosol layer ($\omega_0 = 0.87$, $\tau = 0.5$ at $0.55\ \mu\text{m}$) at a height of 4.2 km along with a thick underling cloud layer (COD = 20) at a height of 1.8 km for the tropical environment similar as our research domain, the simulated atmospheric column heating rates can increase in an average of 3.5 K/day compared to aerosol-free cloudy sky based on RT model calculations under various solar zenith angles. This raise of column radiative heating rates due to SW ARE under AAC conditions can be doubled if we increase the AOD value to 1.0. More accurate estimations for the diurnal variations of above-cloud AREs and their effects on heating rates can be acquired by integrating geostationary satellite observations (e.g., SEVIRI onboard Meteosat) into RT model computations. Y. Y. Chang and S. A. Christopher, Identifying Aerosols above Clouds using the Spinning Enhanced Visible and Infrared Imager, *IEEE Transactions on Geoscience and Remote Sensing* (under revision, 2015) have recently developed aerosol above cloud identification algorithms for SEVIRI, which can be further used to conduct measurement-based estimations of diurnal above cloud AREs and to further constrain climate model simulations.

3.2. Sensitivity and Uncertainties of ARE Estimations During AAC Events

The sensitivity of ARE to changes in ω_0 values for aerosols is further studied by using the four-stream radiative-transfer model. This is done by computing TOA SW fluxes for various COD values with different AAC cases under same atmospheric and surface conditions. Table 2 lists the SW flux and ARE due to AAC as functions of COD and aerosol single scattering albedo (ω_0 at $0.55\ \mu\text{m}$). Means and standard deviations of fluxes in each bin are calculated by an interval of 1 COD bin. When compared with SW flux values of regions dominated by smoke or pure soot aerosols with lower ω_0 values, higher ω_0 values of aerosol (e.g., sea salt) above clouds lead to higher TOA shortwave flux values. Under the same cloud and surface conditions, the signs and magnitudes of AREs for AAC can be largely determined by the variations of aerosols optical properties, which are shown to change from negative (cooling) to positive (warming) values along with the decrease of ω_0 values from 0.98 to 0.85 at $0.55\ \mu\text{m}$. The mean and standard deviations of both SW flux and ARE are calculated based on results for each COD bin. Using smoke aerosols as an example, the sensitivity of ARE to cloud properties can be seen in Table 2 where the largest intervals of $20 < \tau < 32$ with 12 COD bins showed similar standard deviations of SW AREs ($\pm 4.7\text{ Wm}^{-2}$) with corresponding value of $\pm 3.2\text{ Wm}^{-2}$ for the small intervals of $0 < \tau < 2$ with only 2 COD bins. Hence, the AREs are shown to be more sensitive to lower COD values than higher

Table 2. Top of Atmosphere Shortwave Direct Radiative Effect of Aerosols Above Clouds From 4-Stream RT Model^a

Cloud Optical Depth	F _{clr}	ω_0 at 0.55 μm = 0.98 (case 1: sea salt)		ω_0 at 0.55 μm = 0.91 (case 2: smokes)		ω_0 at 0.55 μm = 0.85 (case 3: soot)	
		F _{aer+cld}	SWARE	F _{aer+cld}	SWARE	F _{aer+cld}	SWARE
0–2	176.3 ± 21.5	228.6 ± 4.4	−52.3 ± 4.4	214.1 ± 24.7	−37.8 ± 3.2	176.4 ± 23.5	−0.1 ± 1.9
2–4	245.3 ± 26	301.4 ± 1	−56.1 ± 1	283.9 ± 24	−38.6 ± 1.9	243.5 ± 23.3	1.8 ± 2.6
4–6	316.7 ± 24.1	367.5 ± 2.5	−50.8 ± 2.5	347.5 ± 20.8	−30.8 ± 3.3	305.4 ± 20.3	11.3 ± 3.8
6–8	380.2 ± 20.7	423.7 ± 2.6	−43.5 ± 2.6	401.5 ± 17.5	−21.3 ± 3.3	358.1 ± 17	22.1 ± 3.8
8–12	457.1 ± 29.5	490.5 ± 3.9	−33.5 ± 3.9	465.6 ± 24.5	−8.6 ± 5	420.4 ± 23.7	36.7 ± 5.7
12–20	563.6 ± 35.3	583 ± 4.6	−19.4 ± 4.6	554 ± 29.2	9.6 ± 6	505.6 ± 28.1	58 ± 7.2
20–32	668.2 ± 28.2	674.4 ± 3.4	−6.3 ± 3.4	640.9 ± 23.4	27.3 ± 4.7	588.5 ± 22.2	79.7 ± 5.9

^aThe first column shows the cloud optical depth ranges used in the RT model for the top of the atmosphere (TOA) flux calculations. F_{clr} is the aerosol-free cloudy sky shortwave flux at TOA. F_{aer+cld} is the aerosol-polluted cloudy sky shortwave flux at TOA. SWARE is the SW direct aerosol radiative effect for aerosols above clouds at TOA. Ocean surface and default tropical atmospheric profiles are assumed as background condition. The aerosol optical depth at 0.55 μm is assumed to be 1.0. The heights of aerosol and cloud layer are assumed to be 4.2 km and 1.8 km, respectively. The mean ± stand deviations are calculated based on the values among COD bins.

COD values. A previous study has also indicated higher TOA reflectance sensitivity to lower COD values with carbonaceous aerosol-laden atmosphere than that to higher COD values [Torres *et al.*, 2012]. Since the accurate optical properties of aerosols over the ocean is very hard to acquire without in situ measurements, previous studies always used aerosol data from near AERONET site observations [e.g., Jethva *et al.*, 2013]. However, those single-scattering albedos of smoke aerosols from the biomass burning source area usually increase during transport, because of the increase of size and more in-organic compositions [Reid *et al.*, 2005a, 2005b]. As can be seen in the results of RT simulations, ignoring the increase of aerosol ω_0 during the transports could overestimate the warming (positive) effects due to aerosols above clouds and also underestimate the critical COD values where the signs of ARE due to AAC changed from negative to positive. In Table 2, critical COD values can be seen at 12–20 for $\omega_0 = 0.91$ case, while the ranges have been reduced to 2–4 bin for extremely absorbing aerosols ($\omega_0 = 0.85$). The critical COD values at 860 nm in this study based on multisensor measurements are found to be 8–12; thus, it reveals absorbing smoke aerosols during AAC events with ω_0 will have between 0.85 and 0.91 but close to 0.91.

The sensitivity and uncertainties have been further investigated in Figure 6. As a major indicator of our measurement-based above-cloud ARE estimation algorithm, the simulated aerosol index is found to be sensitive to preassumed cloud, aerosol properties, and layer heights of clouds in Figures 6a and 6b, respectively. Consistent with both previous studies and the collocated observations in Figure 4b, steadily increasing absorbing UV AI can be seen along with increasing underlying COD for a specific AOD value, while two or three times larger AI magnitude can be seen in the higher COD range over 20 than the same amount of aerosols over lower COD values between 0 and 4 [Torres *et al.*, 2012]. Keeping most parameters same as the preceding analysis, about 25% decrease in AI values above cloud layer (COD = 20) can be found in Figure 6b along with the top height of cloud layer changed from 1.0 km to 4.0 km. Similarly, the effects of aerosol layer height on AI values have also been demonstrated based on measurements and RT calculations over both cloud free and cloudy sky [Torres *et al.*, 1998; De Graaf *et al.*, 2005; Torres *et al.*, 2012]. Increasing the height of aerosol layer from 2.5 km to 5.0 km can produce 30% increase in AI magnitudes for a thick underlying cloud layer (COD = 20) located between 1.0 and 1.5 km [Torres *et al.*, 2012]. Combining these simulated results, it can be summarized that the above-cloud AI is associated with aerosol-cloud height difference in the boundary layer under 5 km. The increase of aerosol-cloud layer height distance can apparently cause increasing AI magnitude around 30%. In Figure 6c, we varied 0.55 μm AOD values from 0.1 to 3.0 to build the quantitative correlations between AI and above-cloud SW ARE based on various solar zenith angles. The SW ARE can increase with increasing AI values among all SZAs. For a COD value of 20, SW ARE associated with a highly absorbing aerosol layer (e.g., AI = 2.0) in SZA ranging from 0° to 60° can largely reduce from 50 to 0 Wm^{-2} . Higher SZA will cause lower SW ARE due to specific AAC events.

Uncertainties for measurement-based evaluation of absorbing aerosols above-cloud ARE can be due to the following:

1. TOA SW flux of aerosol-free cloud scene could be estimated with uncertainties based on the linear approximations of TOA SW fluxes and AI for various COD bins from multisensory measurements.

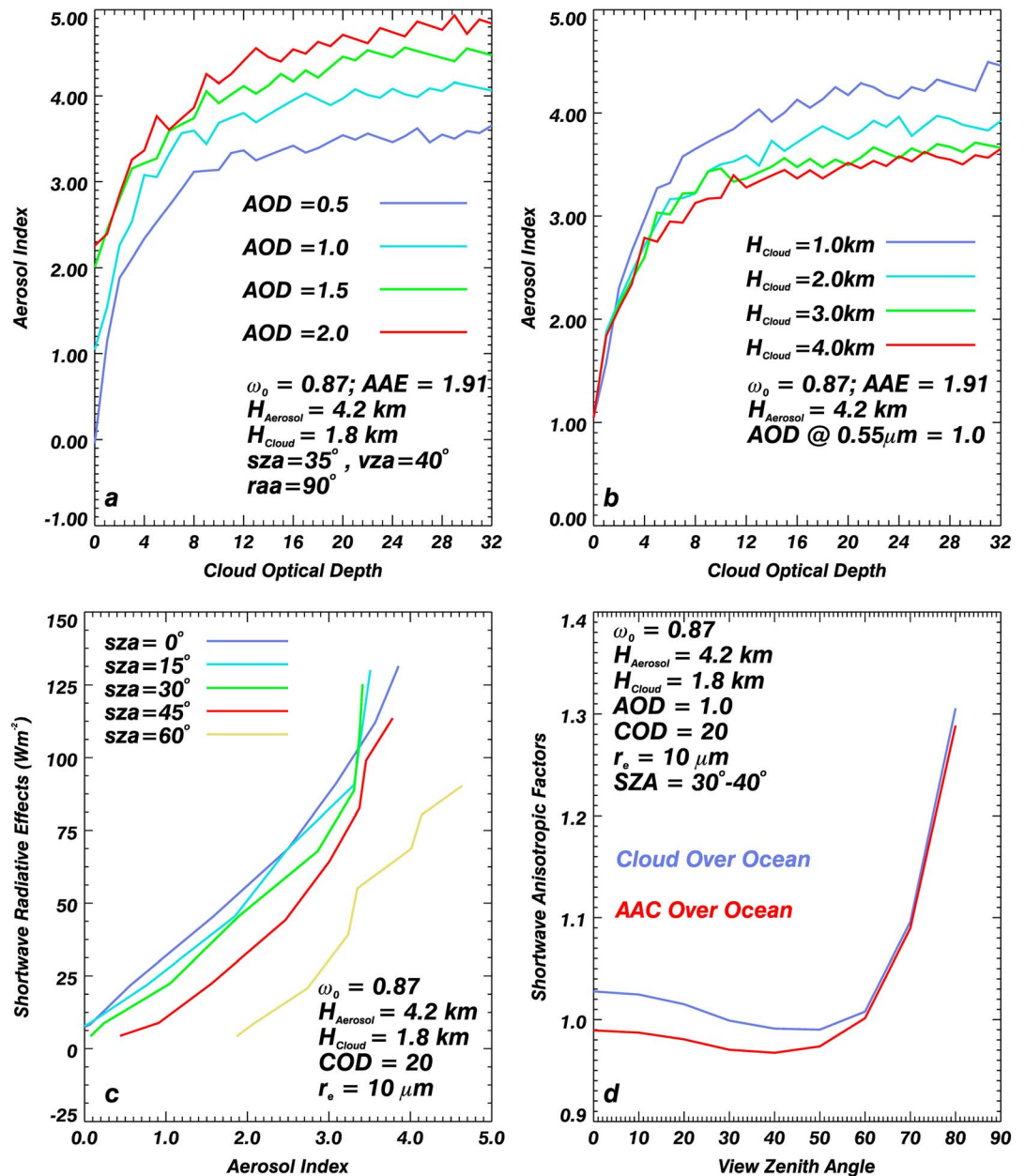


Figure 6. The simulated AI for absorbing aerosols over cloud layer for increasing COD (shown at $0.66 \mu m$) with (a) various AOD at $0.55 \mu m$ from 0.5 to 2.0; (b) various cloud layer height from 1.0 km to 4.0 km; (c) the simulated SW ARE due to AAC events for increasing aerosol index with various SZA from 0° to 60° ; and (d) comparisons of the simulated SW anisotropic factors between AAC events and pure cloud over ocean for various view zenith angles. All other associated parameters have been shown in all figures.

2. MODIS retrieved COD for AAC events could be underestimated due to the absence of absorbing aerosol properties and layer height information in their retrieval process.
3. Another source of uncertainty came from the angular distribution models (ADM) or anisotropic factors used in CERES to convert radiance into radiative fluxes. Several approaches have been adopted for developing the empirical ADMs to reduce the errors in CERES instruments [Loeb et al., 2005; Zhang et al., 2005b; Patadia et al., 2011]. Due to the absence of angular distribution models for aerosols over cloudy sky in CERES data set, the shortwave flux of 99% aerosols above clouds pixels used in this study are retrieved from observed shortwave radiance based on angular distribution model for cloudy ocean scene. In Figure 6d, we simulated the anisotropic factors for various view zenith angles based on idealized aerosol

above-cloud events in a specific SZA range (30°–40°), while about 10%–40% difference in SW anisotropic factors between AAC and pure cloud over ocean can be seen especially in small VZA range from 0 to 60 degree. For TOA SW flux from 100 Wm^{-2} to 700 Wm^{-2} for AAC events, the inaccurate ADM can cause about 10–20% overestimations of TOA SW flux estimations for aerosols above cloud pixels.

4. Conclusion

In this paper, we have demonstrated a new technique for estimating the ARE for absorbing aerosols above clouds over the Atlantic Ocean near the Southwest African coast. The A-Train satellite data sets (OMI, MODIS, and CERES) have been synergistically applied to develop an algorithm for above-cloud aerosol identification and to calculate their direct radiative effect. Our study clearly shows that there are strong warming effects of $36.7 \pm 20.5 \text{ Wm}^{-2}$ (regional mean \pm standard deviation) for AAC, which is different in sign with the TOA instantaneous ARE for smoke aerosols above clear sky (-4 to -36 Wm^{-2}) based on previous studies over the same area. The 660 nm COD values of 8–12 have been identified as the critical values above (below) which aerosol absorbing (scattering) effect dominates and produces positive (negative) AREs over the study area. The ARE values are shown to be more sensitive to aerosols above lower COD values than cases for higher COD values. If these absorbing aerosols above-cloud events due to biomass burning activities are indeed frequent and significant, it can thus offset the shortwave cooling effect of other types of aerosols over cloud-free regions. There are still significant discrepancies between the model simulations and the measurement-based estimations due to inaccurate simulations of aerosols and clouds properties. To reduce the uncertainties in the ARE calculations of AAC, more detailed aerosol properties are needed from in situ measurements. Further research on developing angular distribution model types of AAC is also needed to fully utilize the strengths of the CERES data sets.

Acknowledgments

The CERES data for this paper was obtained through the NASA Langley Distributed Active Archive Systems (<http://ceres-tool.larc.nasa.gov/ord-tool/products?CERESProducts=SSFlevel2>). Data set: CERES SSF. Data set name: CER_SSF_Aqua-FM3-MODIS_Edition3A_301300.200608XXXX. OMI data are available at NASA Goddard Earth Sciences Data and Information Services Center (http://disc.sci.gsfc.nasa.gov/Aura/data-holdings/OMI/omaeruv_v003.shtml). Data set: OMAERUV. Data set name: OMI-Aura_L2-OMAERUV_2006m0801t1112-o10881_v003-2012m0322t034204.SUB.he5. MODIS data are available at NASA Level1 and Atmosphere Archive and Distribution System (<http://lads-web.nascom.nasa.gov/data/>). Data set: MYD06. Data set name: MYD06_L2.A2006213.0050.006.2014041151300.hdf. We thank the principal investigators and associated staffs for establishing and maintaining the AERONET sites over South Africa used in this investigation. This work is supported by NASA Headquarters under the NASA Earth and Space Science Fellowship Program—grant NNX13AN55H. This research is also supported by NASA's radiation sciences and CALIPSO programs.

References

- Ackerman, S. A., C. C. Moeller, K. I. , H. E. Gerber, L. E. Gurnley, W. P. Menzel, and S. C. Tsay (1998), Retrieval of effective microphysical properties of clouds: A wave cloud case study, *Geophys. Res. Lett.*, *25*(8), 1121–1124, doi:10.1029/98GL00042.
- Alfaro-Contreras, R., J. Zhang, J. R. Campbell, R. E. Holz, and J. S. Reid (2014), Evaluating the impact of aerosol particles above cloud on cloud optical depth retrievals from MODIS, *J. Geophys. Res. Atmos.*, *119*, 5410–5423, doi:10.1002/2013JD021270.
- Alfaro-Contreras, R., J. Zhang, J. R. Campbell, and J. S. Reid (2015), Investigating the frequency and trends in global above-cloud aerosol characteristics with CALIOP and OMI, *Atmos. Chem. Phys. Discuss.*, *15*, 4173–4217, doi:10.5194/acpd-15-4173-2015.
- Baum, B. A., W. P. Menzel, R. A. Frey, D. C. Tobin, R. E. Holz, S. A. Ackerman, A. K. Heidinger, and P. Yang (2012), MODIS cloud-top property refinements for collection 6, *J. Appl. Meteor. Climatol.*, *51*, 1145–1163, doi:10.1175/JAMC-D-11-0203.1.
- Chand, D., T. L. Anderson, R. Wood, R. J. Charlson, Y. Hu, Z. Liu, and M. Vaughan (2008), Quantifying above-cloud aerosol using spaceborne lidar for improved understanding of cloudy-sky direct climate forcing, *J. Geophys. Res.*, *113*, D13206, doi:10.1029/2007JD009433.
- Christopher, S. A., and J. Zhang (2002), Shortwave aerosol radiative forcing from MODIS and CERES observations over the oceans, *Geophys. Res. Lett.*, *29*(18), 1859, doi:10.1029/2002GL014803.
- Christopher, S. A., D. V. Kliche, J. Chou, and R. M. Welch (1996), First estimates of the radiative forcing of aerosols generated from biomass burning using satellite data, *J. Geophys. Res.*, *101*, 21,265–21,273, doi:10.1029/96JD02161.
- De Graaf, M., P. Stammes, O. Torres, and R. B. A. Koelmeijer (2005), Absorbing aerosol index: Sensitivity analysis, application to GOME and comparison with TOMS, *J. Geophys. Res.*, *110*, D01201, doi:10.1029/2004JD005178.
- De Graaf, M., L. G. Tilstra, P. Wang, and P. Stammes (2012), Retrieval of the aerosol direct radiative effect over clouds from spaceborne spectrometry, *J. Geophys. Res.*, *117*, D07207, doi:10.1029/2011JD017160.
- De Graaf, M., N. Bellouin, L. G. Tilstra, J. Haywood, and P. Stammes (2014), Aerosol direct radiative effect of smoke over clouds over the southeast Atlantic Ocean from 2006 to 2009, *Geophys. Res. Lett.*, *41*, 7723–7730, doi:10.1002/2014GL061103.
- Eck, T. F., et al. (2013), A seasonal trend of single scattering albedo in southern African biomass-burning particles: Implications for satellite products and estimates of emissions for the world's largest biomass-burning source, *J. Geophys. Res. Atmos.*, *118*, 6414–6432, doi:10.1002/jgrd.50500.
- Feng, N., and S. A. Christopher (2014), Clear sky direct radiative effects of aerosols over Southeast Asia based on satellite observations and radiative transfer calculations, *Remote Sens. Environ.*, *152*, 333–344.
- Fu, Q., and K. N. Liou (1993), Parameterization of the radiative properties of cirrus clouds, *J. Atmos. Sci.*, *50*, 2008–2025.
- Haywood, J. M., S. R. Osborne, and S. J. Abel (2004), The effect of overlying absorbing aerosol layers on remote sensing retrievals of cloud effective radius and cloud optical depth, *Q. J. R. Meteorol. Soc.*, *130*(598), 779–800.
- Hsu, N. C., J. R. Herman, O. Torres, B. N. Holben, D. Tanre, T. F. Eck, and F. Lavenu (1999), Comparisons of the TOMS aerosol index with Sun-photometer aerosol optical thickness: Results and applications, *J. Geophys. Res.*, *104*(D6), 6269–6279, doi:10.1029/1998JD200086.
- Hsu, N. C., J. R. Herman, and S. C. Tsay (2003), Radiative impacts from biomass burning in the presence of clouds during boreal spring in Southeast Asia, *Geophys. Res. Lett.*, *30*(5), 1224, doi: 10.1029/2002GL016485.
- Jethva, H., O. Torres, L. A. Remer, and P. K. Bhartia (2013), A color ratio method for simultaneous retrieval of aerosol and cloud optical thickness of above-cloud absorbing aerosols from passive sensors: Application to MODIS measurements, *IEEE Trans. Geosci. Remote Sens.*, *51*(7), 3862–3870.
- Kacenelenbogen, M., J. Redemann, M. A. Vaughan, A. H. Omar, P. B. Russell, S. Burton, R. R. Rogers, R. A. Ferrare, and C. A. Hostetler (2014), An evaluation of CALIOP/CALIPSO's aerosol above cloud detection and retrieval capability over North America, *J. Geophys. Res. Atmos.*, *119*, 230–244, doi:10.1002/2013JD020178.
- King, M. D., S. C. Tsay, S. E. Platnick, W. Menghua, and K. N. Liou (1997), Cloud retrieval algorithm for MODIS: Optical thickness, effective particle radius, and thermodynamic phase, Algorithm Theor. Basis Doc. ATBD-MOD-05, NASA Goddard Space Flight Cent., Greenbelt, Md.

- Krotkov, N. A., P. K. Bhartia, J. R. Herman, V. Fioletov, and J. Kerr (1998), Satellite estimation of spectral surface UV irradiance in the presence of tropospheric aerosols: 1. Cloud-free case, *J. Geophys. Res.*, *103*(D8), 8779–8793, doi:10.1029/98JD00233.
- L'Ecuyer, T. S., and J. Jiang (2010), Touring the atmosphere aboard the A-Train, *Phys. Today*, *63*, 36–41.
- Liu, Z., M. A. Vaughan, D. M. Winker, C. A. Hostetler, L. R. Poole, D. Hlavka, W. Hart, and M. McGill (2004), Use of probability distribution functions for discriminating between cloud and aerosol in lidar backscatter data, *J. Geophys. Res.*, *109*, D15202, doi:10.1029/2004JD004732.
- Loeb, N. G., S. Kato, K. Loukachine, and N. Manalo Smith (2005), Angular distribution models for top of atmosphere radiative flux estimation from the clouds and the earth's radiant energy system instrument on the Terra satellite. Part I: Methodology, *J. Atmos. Oceanic Technol.*, *22*, 338–351, doi:10.1175/JTECH1712.1.
- McClatchey, R. A., R. W. Fenn, J. E. A. Selby, F. E. Volz, and J. S. Garing (1971), Optical properties of the atmosphere, *Environ. Res. Pap.* 354, Air Force Cambridge Res. Lab, Bedford, Mass.
- Meyer, K., S. Platnick, L. Oreopoulos, and D. M. Lee (2013), Estimating the direct radiative effect of absorbing aerosols overlying marine boundary layer clouds in the southeast Atlantic using MODIS and CALIOP, *J. Geophys. Res. Atmos.*, *118*, 4801–4815, doi:10.1002/jgrd.50449.
- Min, M., and Z. Zhang (2014), On the influence of cloud fraction diurnal cycle and sub-grid cloud optical thickness variability on all-sky direct aerosol radiative forcing, *J. Quant. Spectros. Radiat. Transfer*, *142*, 25–36, doi:10.1016/j.jqsrt.2014.03.014.
- Oh, H.-R., Y.-S. Choi, C.-H. Ho, and M.-J. Jeong (2013), Estimation of aerosol direct radiative effects for all-sky conditions from CERES and MODIS observations, *J. Atmos. Sol. Terr. Phys.*, *102*, 311–320, doi:10.1016/j.jastp.2013.06.009.
- Patadia, F., P. Gupta, S. A. Christopher, and J. S. Reid (2008), A multisensor satellite-based assessment of biomass burning aerosol radiative impact over Amazonia, *J. Geophys. Res.*, *113*, D12214, doi:10.1029/2007JD009486.
- Patadia, F., E.-S. Yang, and S. A. Christopher (2009), Does dust change the clear sky top of atmosphere shortwave flux over high surface reflectance regions? *Geophys. Res. Lett.*, *36*, L15825, doi:10.1029/2009GL039092.
- Patadia, F., S. A. Christopher, and J. Zhang (2011), Development of empirical angular distribution models for smoke aerosols: Methods, *J. Geophys. Res.*, *116*, D14203, doi:10.1029/2010JD015033.
- Peers, F., F. Waquet, C. Cornet, P. Dubuisson, F. Ducos, P. Goloub, F. Szczap, D. Tanre, and F. Thieuleux (2014), Absorption of aerosols above clouds from POLDER/PARASOL measurements and estimation of their direct radiative effect, *Atmos. Chem. Phys. Discuss.*, *14*(18), 25,533–25,579, doi:10.5194/acpd-14-25533-2014.
- Peters, K., J. Quaas, and N. Bellouin (2011), Effects of absorbing aerosols in cloudy skies: A satellite study over the Atlantic Ocean, *Atmos. Chem. Phys.*, *11*, 1393–1404.
- Reid, J. S., R. Koppmann, T. F. Eck, and D. P. Eleuterio (2005a), A review of biomass burning emissions part II: Intensive physical properties of biomass burning particles, *Atmos. Chem. Phys.*, *5*(3), 799–825.
- Reid, J. S., T. F. Eck, S. A. Christopher, R. Koppmann, O. Dubovik, D. P. Eleuterio, B. N. Holben, E. A. Reid, and J. Zhang (2005b), A review of biomass burning emissions part III: Intensive optical properties of biomass burning particles, *Atmos. Chem. Phys.*, *5*, 827–849.
- Russell, P. B., R. W. Bergstrom, Y. Shinozuka, A. D. Clarke, P. F. DeCarlo, J. L. Jimenez, J. M. Livingston, J. Redemann, O. Dubovik, and A. Strawa (2010), Absorption Angstrom Exponent in AERONET and related data as an indicator of aerosol composition, *Atmos. Chem. Phys.*, *10*, 1155–1169, doi:10.5194/acp-10-1155-2010.
- Satheesh, S. K., and V. Ramanathan (2000), Large differences in tropical aerosol forcing at the top of the atmosphere and Earth's surface, *Nature*, *405*, 60–63.
- Satheesh, S. K., K. K. Moorthy, S. S. Babu, V. Vinoj, V. S. Nair, S. N. Beegum, C. B. S. Dutt, D. P. Alappattu, and P. K. Kunhikrishnan (2009), Vertical structure and horizontal gradients of aerosol extinction coefficients over coastal India inferred from airborne lidar measurements during the Integrated Campaign for Aerosol, Gases and Radiation Budget (ICARB) field campaign, *J. Geophys. Res.*, *114*, D05204, doi:10.1029/2008JD011033.
- Smith, G. L. (1994), Effects of time response on the point spread function of a scanning radiometer, *Appl. Opt.*, *33*, 7031–7037.
- Torres, O., P. K. Bhartia, J. R. Herman, Z. Ahmad, and J. Gleason (1998), Derivation of aerosol properties from satellite measurements of backscattered ultraviolet radiation: Theoretical basis, *J. Geophys. Res.*, *103*, 17,099–17,110, doi:10.1029/98JD00900.
- Torres, O., R. Decaie, J. P. Veefkind, and G. de Leeuw (2002), OMI aerosol retrieval algorithm, in *OMI Algorithm Theoretical Basis Document Clouds, Aerosols and Surface UV Irradiance*, vol. 3, ATDB-OMI-03, edited by P. Stammes and R. Noordhoek, pp. 81–82. [Available at http://eospsso.gsfc.nasa.gov/eos_homepage/for_scientists/atbd/docs/OMI/ATBD-OMI-%2003.pdf.]
- Torres, O., A. Tanskanen, B. Veihelmann, C. Ahn, R. Braak, P. K. Bhartia, P. Veefkind, and P. Levelt (2007), Aerosols and surface UV products from Ozone Monitoring Instrument observations: An overview, *J. Geophys. Res.*, *112*, D24547, doi:10.1029/2007JD008809.
- Torres, O., H. Jethva, and P. K. Bhartia (2012), Retrieval of aerosol optical depth above clouds from OMI observations: Sensitivity analysis and case studies, *J. Atmos. Sci.*, *69*(3), 1037–1053.
- Vaughan, M., S. Young, D. Winker, K. Powell, A. Omar, Z. Liu, Y. Hu, and C. Hostetler (2004), Fully automated analysis of space-based lidar data: An overview of the CALIPSO retrieval algorithms and data products, *Proc. SPIE*, *5575*, 16–30.
- Wang, J., and S. A. Christopher (2006), Mesoscale modeling of Central American smoke transport to the United States: 2. Smoke radiative impact on regional surface energy budget and boundary layer evolution, *J. Geophys. Res.*, *111*, D14592, doi:10.1029/2005JD006720.
- Wielicki, B. A., B. R. Barkstrom, E. F. Harrison, R. B. Lee III, G. L. Smith, and J. E. Cooper (1996), Clouds and the Earth's Radiant Energy System (CERES): An Earth observing system experiment, *Bull. Am. Meteorol. Soc.*, *77*, 853–868.
- Wilcox, E. M. (2012), Direct and semi-direct radiative forcing of smoke aerosols over clouds, *Atmos. Chem. Phys.*, *12*(1), 139–149.
- Winker, D. M., M. A. Vaughan, A. Omar, Y. Hu, K. A. Powell, Z. Liu, W. H. Hunt, and S. A. Young (2009), Overview of the CALIPSO mission and CALIOP data processing algorithms, *J. Atmos. Oceanic Technol.*, *26*(11), 2310–2323.
- Winker, D. M., et al. (2010), The CALIPSO mission: A global 3D view of aerosols and clouds, *Bull. Am. Meteorol. Soc.*, *91*, 1211–1229.
- Yu, H. B., and Z. B. Zhang (2013), New directions: Emerging satellite observations of above-cloud aerosols and direct radiative forcing, *Atmos. Environ.*, *72*, 36–40.
- Yu, H. B., Y. Zhang, M. Chin, Z. Y. Liu, A. Omar, L. A. Remer, Y. K. Yang, T. L. Yuan, and J. L. Zhang (2012), An integrated analysis of aerosol above clouds from A-Train multi-sensor measurements, *Remote Sens. Environ.*, *121*, 125–131.
- Zhang, J., S. A. Christopher, L. A. Remer, and Y. J. Kaufman (2005a), Shortwave aerosol radiative forcing over cloud-free oceans from Terra: 2. Seasonal and global distributions, *J. Geophys. Res.*, *110*, D10524, doi:10.1029/2004JD005009.
- Zhang, J., S. A. Christopher, L. A. Remer, and Y. J. Kaufman (2005b), Shortwave aerosol cloud-free radiative forcing from terra: I. Angular models for aerosols, *J. Geophys. Res.*, *110*, D10523, doi:10.1029/2004JD005008.
- Zhang, Z., K. Meyer, S. Platnick, L. Oreopoulos, D. Lee, and H. Yu (2014), A novel method for estimating shortwave direct radiative effect of above-cloud aerosols using CALIOP and MODIS data, *Atmos. Meas. Tech.*, *7*(6), 1777–1789, doi:10.5194/amt-7-1777-2014.